The Astrophysical Journal, 997:194 (8pp), 2026 February 1 https://doi.org/10.3847/1538-4357/ae2d4f

Can Dwarf Spheroidal Galaxies Host a Central Black Hole?

K. Aditya[1] and A. Mangalam[1,2]
[1] Indian Institute of Astrophysics, Koramangala, Bengaluru 560 034, India; kaditya.astro@gmail.com, mangalam@iiap.res.in
[2] Faculty of Physical Sciences, Academy of Scientific and Innovative Research (AcSIR), India
Received 2025 July 7; revised 2025 December 5; accepted 2025 December 7; published 2026 January 22

Abstract

We construct mass models of Milky Way dwarf spheroidal galaxies to place constraints on the central black hole masses they can host. We model the galaxies as a three-component system consisting of the stars, dark matter halo, and a central black hole, using the Osipkov–Merritt–Cuddeford class of the anisotropic distribution function. The posterior distribution of black hole mass remains flat toward the low-mass end, indicating that the kinematic data places an upper limit on the black hole mass. Our analysis yields a 95% credible upper limit of $\log(M_\bullet/M_\odot) < 6$. We combine our results with black hole mass measurements and upper limits from the literature to construct a unified $M_\bullet$–σ_* relation spanning $\sigma_* \sim 10$–$300\,\mathrm{km\,s^{-1}}$, described by $\log(M_\bullet) = 8.32 + 4.08\log(\sigma_*/200\ \mathrm{km\ s^{-1}})$, with an intrinsic scatter of $\sigma_{\rm int} = 0.55$. We compare the inferred limits to models of black hole growth via momentum-driven accretion and stellar capture, which predict black hole masses in the range 10^3–$10^4\,M_\odot$ for the range $\sigma_* \sim 6$–$12\,\mathrm{km\,s^{-1}}$, in close agreement with the $M_\bullet$–σ_* relation within the 95% credible upper limits on the black hole masses derived in this work.

Unified Astronomy Thesaurus concepts: Galaxy dynamics (591)

1. Introduction

The dwarf spheroidal galaxies in the Local Group are simple dynamical systems and are ideal test beds for studying the structure and dynamics of a dark matter halo. The dwarf spheroidal galaxies have relatively high stellar velocity dispersion (M. G. Walker et al. 2007) compared to their luminosity ($M_{\rm Dyn}/L_{\rm V} > 10$; M. Mateo 1998; A. W. McConnachie 2012; G. Battaglia & C. Nipoti 2022), indicating that these galaxies are dominated by dark matter (M. G. Walker 2014). Across our sample, the central velocity dispersions lie in the range 6–11 $\mathrm{km\,s^{-1}}$ (median 8.5 $\mathrm{km\,s^{-1}}$), while at the outermost measured radii, they range from 5 $\mathrm{km\,s^{-1}}$ to 12.1 $\mathrm{km\,s^{-1}}$ (median 7.5 $\mathrm{km\,s^{-1}}$). Further, the ratio of the H I mass to the dynamical mass is equal to $M_{\rm HI}/M_{\rm Dyn} = 10^{-5}$ (J. Grcevich & M. E. Putman 2009; K. Spekkens et al. 2014), indicating that the dwarf spheroidal galaxies are extremely gas-poor. Thus, the relative simplicity of the dwarf spheroidal galaxies means that they can be modeled as a simple collisionless system consisting of *stars + dark matter* without introducing the complexities brought about by the collisional gas component. Further, the dwarf spheroidal galaxies lie within the virial radius (<300 kpc) of the Milky Way, providing detailed kinematics of the tracers and, thus, stringent constraints on the structure of a dark matter halo. The dwarf spheroidal galaxies have a common universal mass scale equal to $M_{300} \simeq 10^7 M_\odot$, within 300 pc, which sets the lower limit on the mass of the dark matter needed for galaxy formation (L. E. Strigari et al. 2008; M. G. Walker et al. 2009) making them ideal systems for studying galaxy formation at the smallest scales.

Recent studies have shown that, apart from the presence of dark matter and stars, dwarf spheroidal galaxies may also potentially host black holes at their centers. In a recent study, M. J. Bustamante-Rosell et al. (2021) show that the dwarf spheroidal galaxy Leo-1 hosts a central black hole with a mass equal to $(3.3 \pm 2.0) \times 10^6 M_\odot$. Also, see R. Pascale et al. (2024), who show that kinematics in the central region may only impose an upper limit equal to $10^5 M_\odot$. Also, interestingly, the black hole mass estimated by M. J. Bustamante-Rosell et al. (2021) for Leo-1 exceeds the values predicted by the standard $M_\bullet$–σ_* relation (J. Kormendy & L. C. Ho 2013). Furthermore, using deep radio observations, T. J. Maccarone et al. (2005) find the signature of the $10^4 M_\odot$ black hole in the Ursa Minor (UM) dwarf spheroidal galaxy, also see V. Lora et al. (2009). In another study, using deep XMM Newton observations, L. Manni et al. (2015) find an upper limit on the black hole mass equal to $2.3 \times 10^6 M_\odot$ in UM. J. R. Jardel & K. Gebhardt (2012), using Schwarzschild orbit superposition models, find an upper limit on black hole mass in another dwarf spheroidal galaxy, Fornax, equal to $3.2 \times 10^4 M_\odot$. For the remaining dwarf spheroidal galaxies in our sample, Carina, Draco, Leo II, Sculptor, and Sextans, no direct measurements or upper limits on central black hole masses have been reported in the literature. Further studies by A. E. Reines et al. (2013), J. M. Bellovary et al. (2019), and A. E. Reines (2022) provide compelling observational evidence for black holes in the low-mass dwarf galaxies.

In this paper, we construct dynamical models of dwarf spheroidal galaxies as *stars + dark matter + black hole* and constrain the black hole mass in conjunction with the parameters corresponding to the dark matter halo. We model the dwarf spheroidal galaxies using the Osipkov–Merritt–Cuddeford class of anisotropic distribution functions (L. Osipkov 1979; D. Merritt 1985; P. Cuddeford 1991). Distribution function-based models have been extensively employed to derive dynamical constraints on the properties of dark matter halos and central black holes. For spherical distribution function models, see L. Posti et al. (2015), R. Pascale et al. (2019), G. Shchelkanova et al. (2021), and K. Aditya (2024), and for axisymmetric distribution function models of galaxies, see K. Aditya & A. Banerjee (2021) and K. Aditya et al. (2022, 2023). We use a publicly available stellar dynamics toolbox called Action-based Galaxy Modelling Architecture (AGAMA; E. Vasiliev 2019) to compute the

distribution function and other associated quantities like the line-of-sight velocity dispersion. We will derive the constraints on the black hole masses and inspect possible formation scenarios for black holes in dwarf spheroidal galaxies. Finally, we will discuss the estimated black hole masses in the context of the unified $M_\bullet$–σ_* relation spanning $\sigma_* \sim 10$–$300\,\mathrm{km\,s^{-1}}$. The $M_\bullet$–σ_* relation in the low-σ_* regime is particularly valuable for current simulations and future searches for intermediate-mass black holes (H. N. Ngo et al. 2025; D. D. Nguyen et al. 2025) using instruments such as LIGER (S. A. Wright et al. 2024) on Keck or HARMONI on the upcoming 39 m Extremely Large Telescope (ELT; N. A. Thatte et al. 2022).

The paper is organized as follows. In Section 2, we introduce the dynamical models of the dwarf spheroidal galaxies, and we present the results and discuss their implications in Section 3. Finally, we draw our conclusions in Section 4.

2. Dynamical Model of the Dwarf Spheroidal Galaxy

We model the dwarf spheroidal galaxy as a collisionless system of stars and dark matter with a central black hole. We use the observed stellar photometry (R. R. Muñoz et al. 2018) of dwarf spheroidal galaxies for constructing the potential of the stellar distribution. Fixing the stellar density from observations alleviates the degeneracy between the stellar and the dark matter distribution, allowing us to place better constraints on the dark matter density profile parameters and the black hole mass. We adopt the structural parameters of the dwarf spheroidal galaxies from R. R. Muñoz et al. (2018), which were measured using a Plummer density profile. In our model, we keep the parameters corresponding to the potential of the dark matter halo and the black hole masses as free parameters. Once we construct the total potential, we numerically compute the stellar distribution function in the total potential and constrain our model parameters using the observed stellar velocity dispersion (M. G. Walker et al. 2007, 2009). We estimate the posterior distribution of our model parameters using *emcee* (D. Foreman-Mackey et al. 2013).

2.1. Stellar Density

We model the stellar density using the Plummer potential (H. C. Plummer 1911) given by,

$$\Phi(r) = -\frac{GM_*}{\sqrt{R^2 + R_*^2}}. \tag{1}$$

The density corresponding to this potential is given by,

$$\rho(r) = \frac{3M_*}{4\pi R_*^3}\left(1 + \frac{R^2}{R_*^2}\right)^{-\frac{5}{2}}. \tag{2}$$

In the above equations, R_* is the scale length of the stellar density and M_* is the mass of the stellar density profile. The parameters corresponding to the stellar density profile of the Milky Way dwarf spheroidal galaxies studied in the current work are taken from R. R. Muñoz et al. (2018) and are summarized in Table 1.

2.2. Dark Matter Density

We model the dark matter density using the Navarro–Frenk–White (NFW) profile (J. F. Navarro et al. 1997) given by,

$$\Phi_{\mathrm{DM}}(R) = -4\pi G\rho_{\mathrm{DM}}R_s^3\frac{\ln\left(1 + \frac{R}{R_s}\right)}{R}. \tag{3}$$

The corresponding density profile is given by,

$$\rho(r) = \frac{\rho_{\mathrm{DM}}}{\frac{R}{R_s}\left(1 + \frac{R}{R_s}\right)^2}. \tag{4}$$

In the above equations, ρ_{DM} and R_s are the density and scale length of the dark matter density profile, respectively.

2.3. Black Hole

We model the black hole as,

$$\Phi_\bullet = \frac{GM_\bullet}{R}, \tag{5}$$

where $M_\bullet$ is the mass of the black hole.

2.4. Galaxy Model

We combine the density of the stellar component and dark matter models to compute the total potential of the system using the `AGAMA` class `Potential`. The `Potential` class in `AGAMA` uses multipole expansion to compute the potential for any given density profile. The density is decomposed into spherical harmonics with radially varying amplitudes. Finally, the potential corresponding to each spherical harmonics term is combined to compute the total potential (see E. Vasiliev 2019). Once the density is defined, the potential can be computed by calling the built-in Poisson solver implemented in `AGAMA` class `Potential`. We define the generalized anisotropic distribution function (L. Osipkov 1979; D. Merritt 1985; P. Cuddeford 1991) given by,

$$f(E, L) = \hat{f}(Q)\,L^{-2\beta_0}, \quad Q = E - L^2/(2R_a^2), \tag{6}$$

where R_a is the anisotropy radius. In the above formula $E = \Psi_T - v^2/2$ is the binding energy, $\Psi_T = -\phi_T$ is the relative total potential due to the combined effect of all the density components, and $f(Q) = 0\ \forall\ Q \leqslant 0$. The term $L^{-2\beta_0}$ regulates the orbital anisotropy. When $\beta_0 = 0$, the distribution function is ergodic, and the orbits are isotropic, whereas $\beta_0 < 0$ and $\beta_0 > 0$ produce distribution functions that describe tangentially and radially biased orbits, respectively. In the Osipkov–Merritt–Cuddeford class of the anisotropic distribution function, the density component depends on the energy and on the angular momentum modulus of stellar orbits through the variable Q. The Q parameter controls the radial variation of anisotropy. The distribution function is ergodic within the anisotropy radius ($r << R_a$) and becomes radially biased beyond the anisotropy radius $r >> R_a$. The parameters of our dynamical model are described in Table 2. The distribution function produces a velocity anisotropy

$$\beta(r) \equiv 1 - \frac{\sigma_T^2}{2\sigma_R^2} = \frac{R^2 + \beta_0 R_a^2}{R_a^2 + R^2}, \tag{7}$$

where σ_{T}^2 and σ_{R}^2 are the tangential and the radial velocity dispersions, respectively. In the above equation, β_0 is the value

Table 1
Observational Data Corresponding to the Dwarf Spheroidal Galaxies

Galaxy	R.A. (J2000) (hh: mm: ss)	Decl. (J2000) (dd: mm: ss)	Distance (kpc)	M_* ($10^6 M_\odot$)	R_* (pc)	References Photometry	References Velocity Dispersion
Carina	06: 41: 36.7	−50: 57: 58	106 ± 6	0.38	308 ± 23	R. R. Muñoz et al. (2018),	M. G. Walker et al. (2007)
Draco	17: 20: 12.4	+57: 54: 55	76 ± 6	0.29	214 ± 2	—"—	—"—
Fornax	02: 39: 59.3	−34: 26: 57	147 ± 12	20	838 ± 3	—"—	—"—
Leo-1	10: 08: 28.1	+12: 18: 23	254 ± 15	5.5	270 ± 2	—"—	—"—
Leo-2	11: 13: 28.8	+22: 09: 06	233 ± 14	0.74	171 ± 2	—"—	—"—
Sculptor	01: 00: 09.4	−33: 42: 33	86 ± 6	2.3	280 ± 1	—"—	—"—
Sextans	10: 13: 03.0	−01: 36: 53	86 ± 4	0.44	413 ± 3	—"—	—"—
UM	15: 08: 08.5	+67: 13: 21	76 ± 3	0.29	407 ± 2	—"—	M. G. Walker et al. (2009)

Table 2
Parameters Describing the Dynamical Model of a Dwarf Spheroidal Galaxy

Symbol	Description
$M_\bullet$	Black hole mass
$M_{\rm DM}$, $\Phi_{\rm DM}$, $\rho_{\rm DM}$	Mass, potential, and density of the dark matter halo
M_*, Φ_*, ρ_*	Mass, potential, and the density of stars
$\phi_T = \phi_\star + \phi_{\rm DM} + \phi_\bullet$	Total potential
$\Psi_{\rm T} = -\phi_{\rm T}$	Relative total potential
R_s	Scale radius of dark matter density profile
R_*	Scale radius of stellar density profile
β_0	Anisotropy at the center
R_a	Anisotropy radius

of anisotropy at the center and R_a is the anisotropy radius. The isotropic case is obtained by setting $\beta_0 = 0, R_a = \infty$. $\hat{f}(Q)$ is obtained through a more general Eddington inversion formula derived by L. Osipkov (1979), D. Merritt (1985), P. Cuddeford (1991), and L. Ciotti (2021). The distribution function is tangentially biased when $\beta_0 < 0$, radially biased when $\beta_0 > 0$, and isotropic when $\beta_0 = 0$. The distribution function $\hat{f}(Q)$ is given by (P. Cuddeford 1991; L. Ciotti 2021),

$$\hat{f}(Q) = \frac{(-1)^{m+1}\cos(\beta_0\pi)}{\pi\, 2^{\beta_0}(2\pi)^{3/2}} \cdot \frac{\Gamma\left(\frac{3}{2} + \beta_0 - m\right)}{\Gamma(1+\beta_0)} \cdot \frac{d}{dQ} \tag{8}$$

$$\times \int_0^Q \frac{d^m\hat{\rho}}{d\Psi_T^m} \cdot \frac{d\Psi_T}{(Q-\Psi_T)^{\frac{3}{2}+\beta_0-m}}. \tag{9}$$

where m is defined as

$$m \equiv \mathrm{int}\left(\beta_0 + \frac{1}{2}\right) + 1. \tag{10}$$

We fix the density of the stellar component directly from observations and calculate the corresponding potential by solving the Poisson's equation using multipole expansion methods implemented in AGAMA class `Potential`. We then combine the potential due to the stellar component with the potential corresponding to the dark matter halo and the black hole. The parameters corresponding to the black hole and the dark matter halo are treated as free parameters in our model, whereas the potential for the stellar component is fixed from the observations. Once the potentials and density for each component are self-consistently defined by solving the Poisson's equation in AGAMA, the distribution function that generates the given density is computed using the `QuasiSpherical` model implemented in the `DistributionFunction` class in AGAMA. The `DistributionFunction` class numerically computes the augmented density $\hat{\rho}(\Psi_T)$ in terms of the potential and computes the corresponding distribution function. In the above equation, Ψ_T is the total relative potential of the system given by $\Psi_T = -\phi_T = \phi_* + \phi_{\rm DM} + \phi_\bullet$. Finally, we combine the density and the distribution function using the AGAMA module `GalaxyModel` and use the task `moments` to compute the line-of-sight velocity dispersion as a function of radius. We compare the modeled velocity dispersion to the observed velocity dispersion using χ^2 defined as

$$\chi^2 = \sum_R \frac{(\sigma_{\rm obs}(R) - \sigma_{\rm model}(R))^2}{s_{\rm err}^2(R)}, \tag{11}$$

where $\sigma_{\rm obs}$ is the observed stellar dispersion, $\sigma_{\rm model}$ is the modeled line-of-sight dispersion, and $s_{\rm err}^2$ is the error on the observed dispersion.

3. Results and Discussion

We computed the posterior probability distribution of the model parameters using the "emcee" Markov Chain Monte Carlo (MCMC) ensemble sampler (D. Foreman-Mackey et al. 2013). We adopted uniform priors on the model parameter:

1. $6.0 < \log(M_{\rm DM}/M_\odot) < 10$
2. $1.0 < \log(M_\bullet/M_\odot) < 7$
3. $-0.5 < \log(R_s/\mathrm{kpc}) < 1.0$
4. $-0.5 < \beta_0 < 0.5$.

The above priors on the model allow us to explore the posterior distribution of dark matter halos ($M_{\rm DM}$, R_s) and black hole masses ($M_\bullet$) over a large parameter range. We sample $M_{\rm DM}$, R_s, and $M_\bullet$ in logarithmic space to ensure uniform sampling of parameters that span several orders of magnitude. Furthermore, log uniform priors assign equal weight to samples per decade and produce a nearly Gaussian posterior distribution. The range of priors also encompasses the stellar distributions with tangentially biased anisotropy ($\beta_0 < 0$), a radially biased anisotropy profile ($\beta_0 > 0$), and isotropic models ($\beta_0 = 0$, $R_a \to \infty$). The bound on $\beta_0 \geqslant -0.5$ is imposed by the implementation of the Osipkov–Merritt–Cuddeford class of anisotropic distribution function in AGAMA. When $\beta_0 < -0.5$, the derivative of the augmented density ($\hat{\rho}(\Psi_T)$) becomes poorly conditioned at the center, and the distribution function becomes numerically unstable. So models implemented in AGAMA are restricted to $\beta_0 > -0.5$, which ensures that the distribution function is physical and numerically stable. Our preliminary fits showed that the inferred values of R_a exceeded the physical extent of the galaxy, indicating that the models exhibit constant velocity anisotropy within

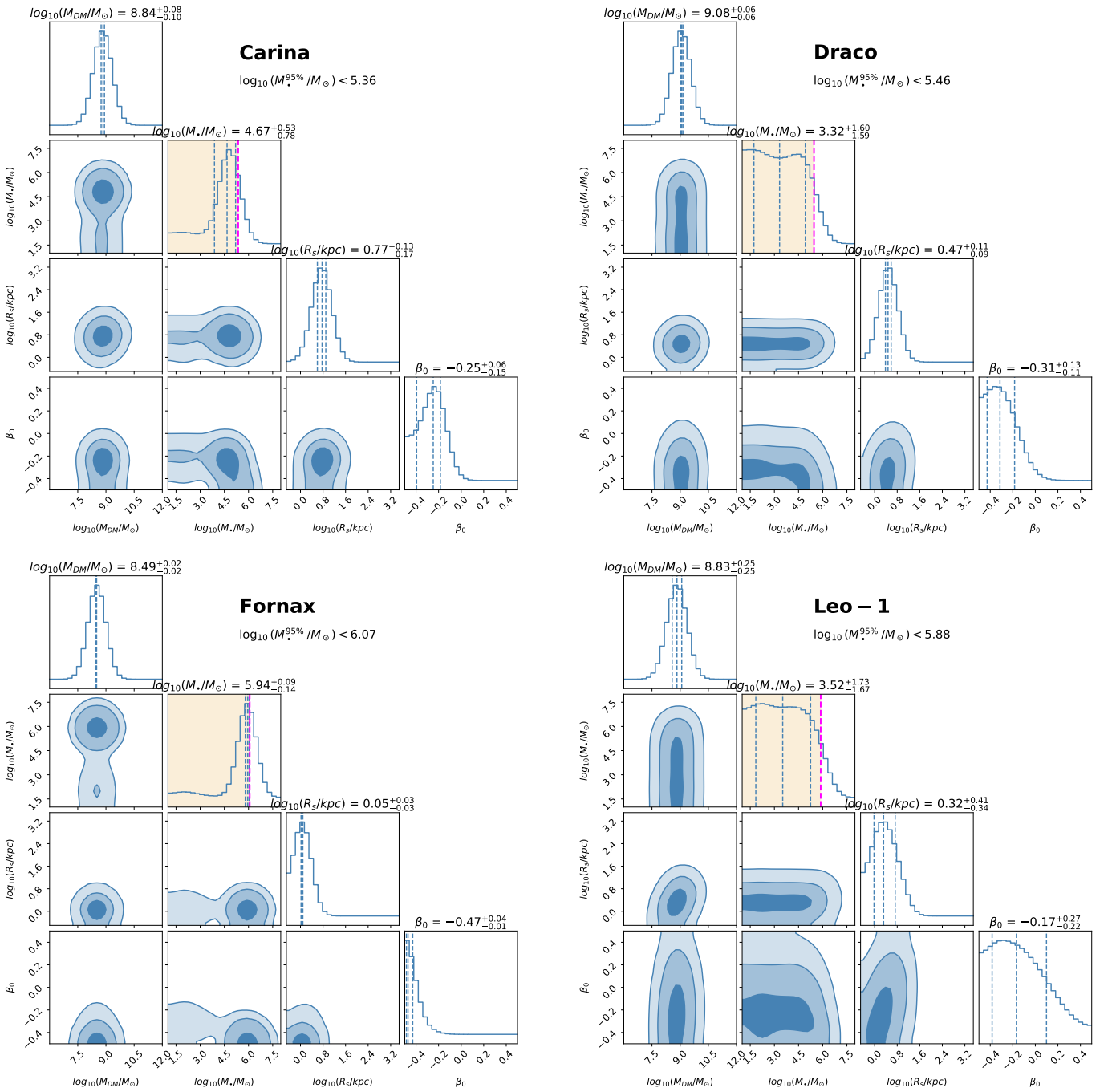

Figure 1. Posterior probability distribution corresponding to model parameters of dwarf spheroidal galaxies: Carina, Draco, Fornax, and Leo-1. The dashed blue lines depict the 16th, 50th, and 84th percentiles of the posterior probability distribution. The posterior distribution for the black hole mass is flat toward the low-mass end and drops off at the 95% credible upper limit of $\log(M_\bullet/M_\odot) < 6$, as indicated by the vertical magenta line.

the kinematic extent of the galaxy. So, we fix the value of $R_a = \infty$. We show the posterior distribution of our model parameters in Figures 1 and 2, respectively. The posterior for the dark matter mass is strongly constrained, with the median value of $\log(M_{\rm DM}/M_\odot)$ lying between 8.3 and 9.1. The dark matter masses for the dwarf spheroidal galaxies are consistent with $\log(M_{300}/M_\odot) = 7$, as estimated by L. E. Strigari et al. (2008), M. G. Walker et al. (2009), and M. G. Walker (2014), and with $\rho_{\rm DM}(150)\,/\,M_\odot\,{\rm kpc}^{-3} = (7\text{–}20) \times 10^7$, in agreement with J. I. Read et al. (2019) and K. Hayashi et al. (2020). The posterior distribution for the dark matter scale length is also well constrained, with values lying in the range $\log(R_s/{\rm kpc}) =$ 0.02-0.8. The posterior for the black hole mass remains flat toward the low-mass end, indicating that the kinematic data only place upper limits on the black hole mass. Therefore, we quote the 95% credible upper limit instead of the median. Our analysis yields 95% credible upper limits in the range $\log(M_\bullet/M_\odot) < 5.1$–6.1 for black hole masses for our sample of dwarf spheroidal galaxies. We overlay the model velocity dispersion profiles corresponding to the 50th and 95th percentiles of the posterior distribution on the observed velocity dispersion data in Figure 3. For comparison, we select a model with $M_\bullet = 10^7\,M_\odot$ from the MCMC chain and overlay its predicted profile on the data. The kinematic data constrain the black hole

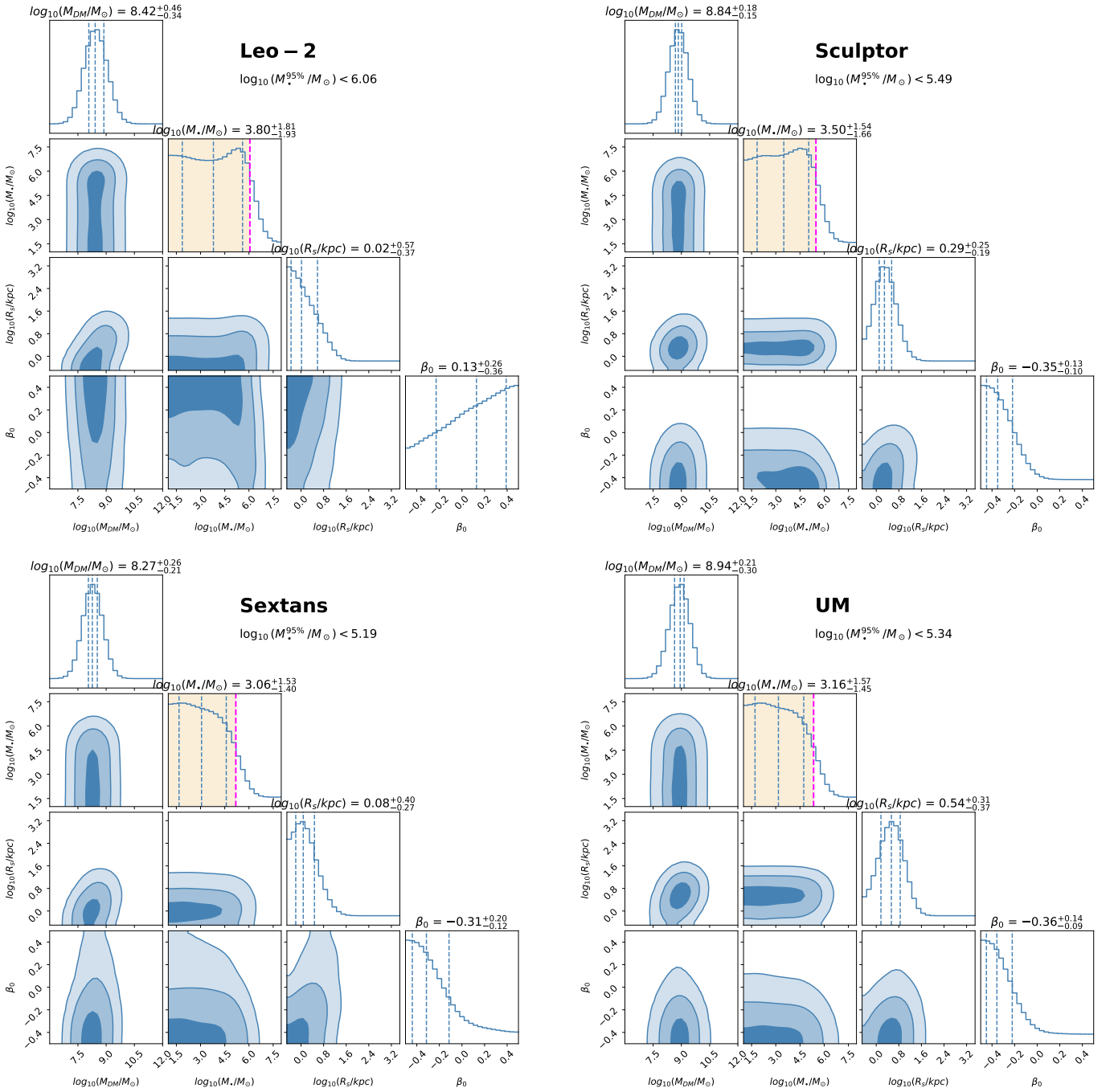

Figure 2. Same as Figure 1, but for the dwarf spheroidal galaxies Leo-2, Sculptor, Sextans, and UM.

mass to be below $10^6\,M_\odot$ within the observed uncertainties, as models with $10^7\,M_\odot$ clearly overpredict the velocity dispersion. The models are tangentially biased, with $\beta_0 < 0$. However, we note that β_0 is unconstrained for Leo-2, likely due to insufficient kinematic data close to the center. The posterior distribution for black hole masses indicates that the dwarf spheroidal galaxies around the Milky Way can at most accommodate an intermediate-mass black hole (IMBH).

3.1. Formation Scenarios for IMBH

It has been shown that the black holes at the center of galaxies grow by accreting gas (A. Soltan 1982; S. Tremaine et al. 2002). A. King (2003) shows that the $M_\bullet$–σ_* relation emerges naturally when the outflows from the black hole can communicate with the ambient medium through exchange of momentum and drive a significant outward flow. If the black hole mass is greater than the ambient medium and the surrounding gas is completely expelled, then the saturation black hole mass (D. Merritt 2013) is given by

$$M_\bullet = 2 \times 10^8 \left(\frac{f_g}{0.1}\right)\left(\frac{\sigma_*}{200\ ^{-1}\mathrm{km\,s}}\right)^4 M_\odot, \tag{12}$$

where f_g is the gas fraction. The black hole mass saturates to the values predicted by the σ^4 law when the outflow velocity exceeds the escape velocity of the medium, driving away the ambient gas and halting the accretion process. Using the value

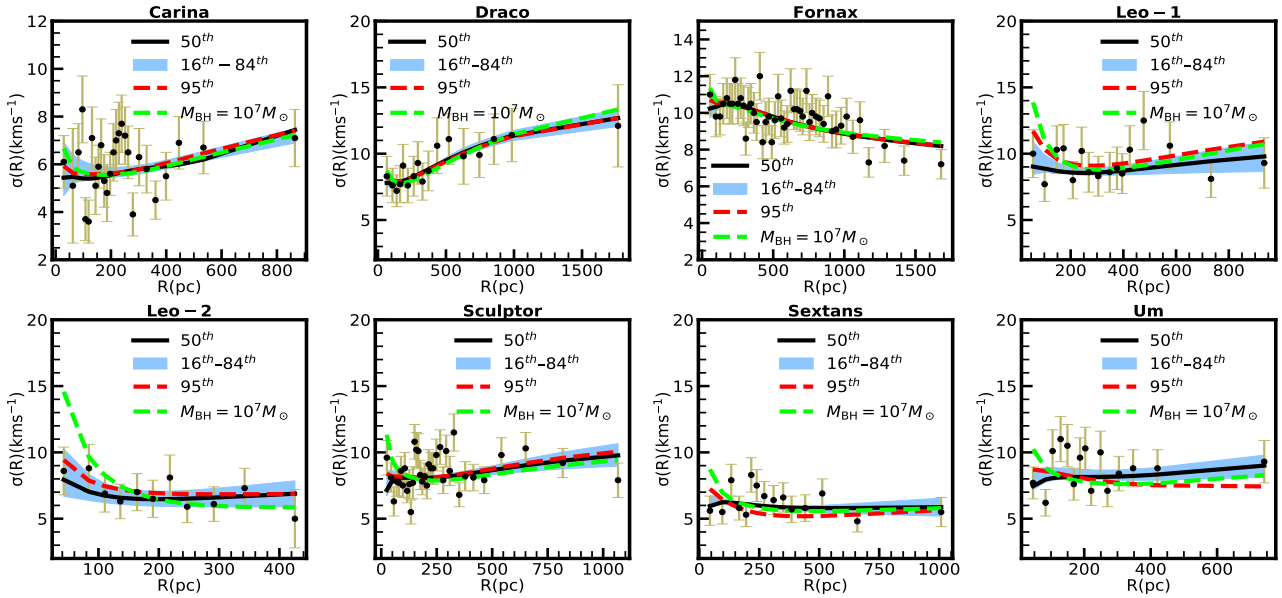

Figure 3. The black line indicates the 50th percentile, and the red curve represents the 95% credible upper limit of the posterior distribution. The blue shaded region indicates the 16th–84th percentile range. The green curve represents a model with $M_\bullet = 10^7\,M_\odot$, selected from the MCMC posterior samples.

of the cosmic baryon fraction $f_g = 0.16$ (E. Komatsu et al. 2009) and typical velocity dispersion for our sample of galaxies in Equation (12), we obtain $M_\bullet \approx 10^3 M_\odot$. The saturation mass typically sets the upper limits on the seed black hole mass in dwarf spheroidal galaxies $\leqslant 10^3 M_\odot$. The critical mass below which the stellar capture dominates over accretion (D. Bhattacharyya & A. Mangalam 2020) is given by

$$M_c = 5 \times 10^3 \eta^{-0.75} M_\odot, \tag{13}$$

where $\eta = \dot{M}_\odot / \dot{M}_E$, $\dot{M}_E$ is the Eddington accretion rate. Assuming sub-Eddington accretion $\eta \geqslant 0.07$, we get critical mass $\approx 10^4 M_\odot$, higher than the saturated black hole mass. Thus, stellar capture may be an important channel through which the black hole can grow in dwarf spheroidal galaxies. It is essential to note that the growth of a black hole due to accretion is halted when the ambient medium is completely expelled. However, the black hole continues to grow by accreting mass, capturing stars, and potentially reaching masses of $10^4\,M_\odot$ and above as shown in D. Bhattacharyya & A. Mangalam (2020: see Equation (74) and Figure 17 for estimates).

3.2. *Unifying the* $M_\bullet$–σ_* *Relation*

The upper limits on the black hole masses derived in this study provide a unique opportunity to extend the $M_\bullet$–σ_* relation in the low mass regime. The unified relation presented in this work spans a wide range of velocity dispersions (10–300 km s^{-1}), bridging both the low-mass and extremely high-mass regimes. The sample includes low-mass black hole measurements from K. Gebhardt et al. (2005), D. E. McLaughlin et al. (2006), R. P. van der Marel & J. Anderson (2010), N. Lützgendorf et al. (2013), S. Kamann et al. (2014), and M. den Brok et al. (2014) and include ultramassive black hole ($M_\bullet > 10^9 M_\odot$) measurements from M. Cappellari et al. (2002), C. Tadhunter et al. (2003), E. Dalla Bontà et al. (2009), N. J. McConnell et al. (2011, 2012), A. Beifiori et al. (2012), S. P. Rusli et al. (2013), K. Gültekin et al. (2014), A. Yıldırım et al. (2015), J. L. Walsh et al. (2016), and J. Thomas et al. (2016). We also add new measurements of ultramassive black hole masses from K. Mehrgan et al. (2019), J. W. Nightingale et al. (2023), and C. R. Melo-Carneiro et al. (2025) to the sample. Current ELT/HARMONI simulations (D. D. Nguyen et al. 2023, 2025; H. N. Ngo et al. 2025) rely on simple prescriptions such as the galaxy–black hole scaling relation (D. Krajnović et al. 2018) for assigning black hole masses. The unified $M_\bullet$–σ_* relation presented in this paper, spanning 7 orders of magnitude, provides a more balanced calibration and offers a stronger empirical foundation for future ELT-based black hole simulations. In order to produce more complete models of the $M_\bullet$–σ relation across all scales, we have to add the effects of tidal stripping to the black hole growth paradigm of D. Bhattacharyya & A. Mangalam (2020) that includes the growth of black hole mass and spin through stellar capture, gas accretion, and mergers in a relativistic framework over cosmic time. This will help us improve the mass limits and constraints across a wider mass range, which we plan to address in a detailed future study.

We construct an extended and heterogeneous sample of black hole masses by assembling measurements from N. Lützgendorf et al. (2013), R. C. van den Bosch (2016), and J. E. Greene et al. (2020), which include black hole masses estimated using stellar and gas dynamics, megamasers, and reverberation mapping. We add the upper limits on black hole masses derived in the present work from stellar dynamics to this extended sample. Our final sample, therefore, contains both direct black hole mass measurements and upper limits. R. C. van den Bosch (2016) report an intrinsic scatter equal to 0.49 ± 0.03 in the $M_\bullet$–σ_* relation for a sample that includes black hole masses estimated using stellar and gas dynamics, megamasers, and reverberation mapping. Similarly, K. Gültekin et al. (2009) constructed a sample using only dynamical methods, excluding black hole masses obtained from reverberation mapping. K. Gültekin et al. (2009) showed that stellar-dynamical and megamaser subsample yields a scatter of 0.49 ± 0.075, whereas the gas-dynamical subsample yields a somewhat smaller value of 0.35 ± 0.096. They also find that pseudobulges exhibit an intrinsic scatter of

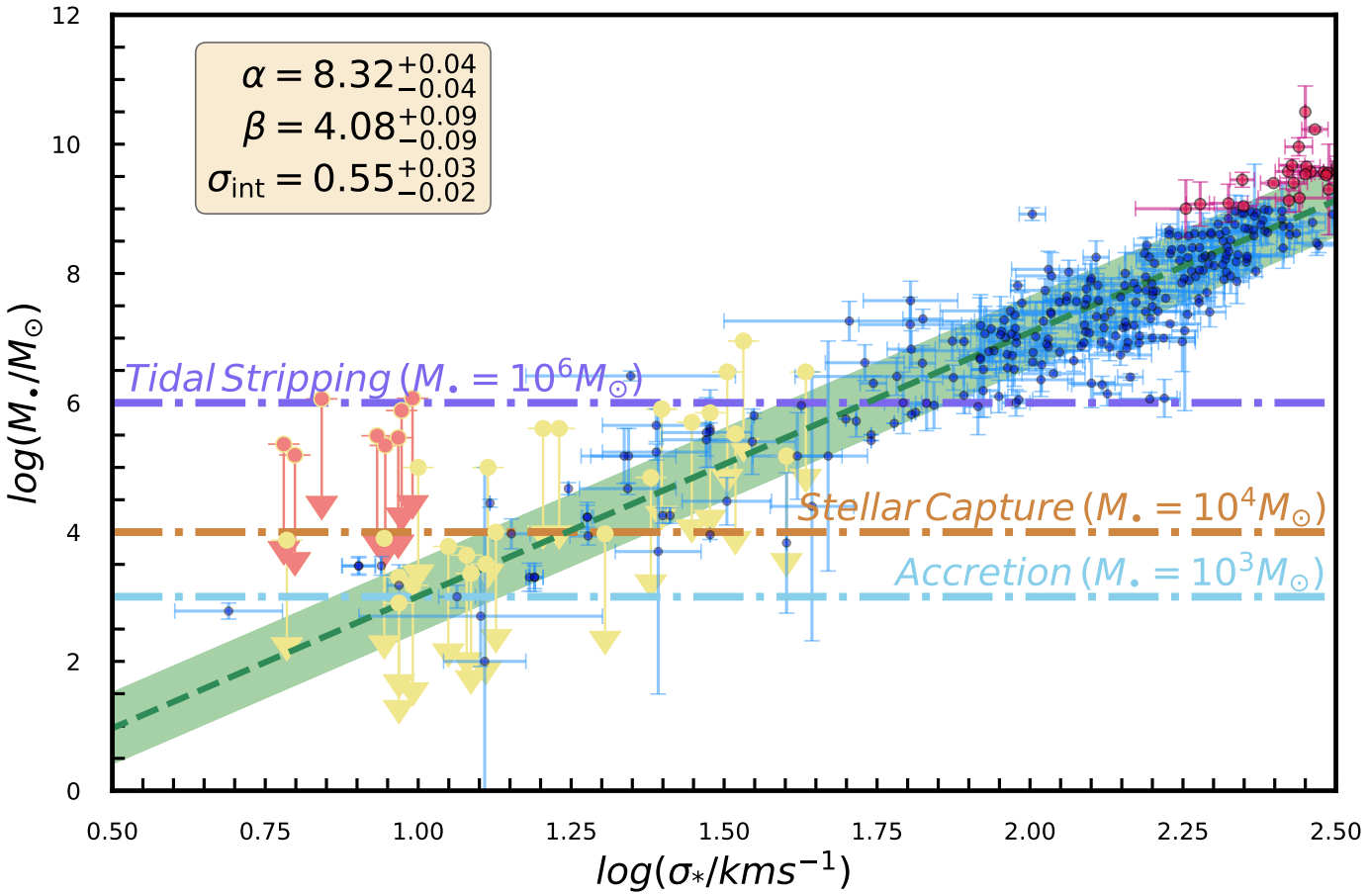

Figure 4. A unified $M_\bullet$–σ_* relation spanning stellar velocity dispersions from ∼10 km s^{-1} to ∼300 km s^{-1}. Blue points represent black hole mass estimates, while yellow arrows denote upper limits, compiled from N. Lützgendorf et al. (2013), R. C. van den Bosch (2016), and J. E. Greene et al. (2020). The red arrows indicate the upper limits obtained in the present work. The green line shows the best-fit regression, and the shaded region indicates 1σ scatter. Magenta points depict ultramassive black holes ($M_\bullet > 10^9$. Theoretical limits on black hole masses (for our sample range $\sigma_* \sim$ 6–12 km s^{-1}) due to accretion, stellar capture, and tidal stripping are also overlaid on the plot for comparison.

0.28 ± 0.096 while their full sample has a scatter of 0.44 ± 0.06. Taken together, these studies indicate that the intrinsic scatter in the $M_\bullet$–σ_* relation typically lies in the range of 0.3–0.6 (K. Gültekin et al. 2009; N. J. McConnell & C.-P. Ma 2013), reflecting the differences in black hole mass measurement techniques, galaxy morphology, and fitting methods. We perform Bayesian linear regression using *emcee* (D. Foreman-Mackey et al. 2013), modeling the likelihood for the censored data via the cumulative distribution function (B. C. Kelly 2007; N. Lützgendorf et al. 2013). We fit our dataset to

$$\log(M_\bullet) = \alpha + \beta \log(\sigma_*/200), \quad (14)$$

and find $\alpha = 8.32^{+0.04}_{-0.04}$, $\beta = 4.08^{+0.09}_{-0.09}$, with an intrinsic scatter equal to $\sigma_{\rm int} = 0.55^{+0.03}_{-0.02}$. We show the unified $M_\bullet$–σ_* relation spanning stellar velocity dispersions from ∼10 km s^{-1} to ∼300 km s^{-1} in Figure 4. We find that the slope of the $M_\bullet$–σ_* relation $\beta = 4.08$ lies within the typical range of $\beta \sim 3.68$–5.35 reported for a diverse population of galaxies (e.g., K. Gebhardt et al. 2000; L. Ferrarese & D. Merritt 2000; D. Merritt & L. Ferrarese 2001; S. Tremaine et al. 2002; A. W. Graham 2008; K. Gültekin et al. 2009; R. C. van den Bosch 2016; D. Bhattacharyya & A. Mangalam 2018). We find an intrinsic scatter of $\sigma_{\rm int} = 0.55^{+0.03}_{-0.02}$ in the $M_\bullet$–σ_* relation, compared to $\sigma_{\rm int} = 0.44 \pm 0.06$ (K. Gültekin et al. 2009) and $\sigma_{\rm int} = 0.49 \pm 0.03$ (R. C. van den Bosch 2016). The increased scatter in our sample could be due to the inclusion of low-mass galaxies and upper limits in the fit.

The $M_\bullet$–σ_* relation presented in this work indicates that dwarf spheroidal galaxies can host black holes with masses in the range of 10^2–$10^3\,M_\odot$, consistent with a scenario where black holes accrete mass by exchanging momentum with the surrounding medium, whereas a black hole can grow through stellar capture up to $10^4\,M_\odot$, even when the accretion-driven growth has stalled. The black hole masses predicted from both stellar capture and gas accretion lie within the upper limits obtained in our study. F. Pacucci et al. (2023) present an alternative scenario for the presence of massive black holes $\sim 10^6 M_\odot$ in dwarf spheroidal galaxies. F. Pacucci et al. (2023) suggest that the progenitors of present-day dwarf spheroidal galaxies, initially hosting stellar masses of $\sim 10^6\,M_\odot$, may have occupied higher positions on the $M_\bullet$–σ_* relation. However, mass loss of up to ∼58% during pericentric passages can significantly reduce their stellar content, shifting them to the lower end of the observed $M_\bullet$–σ_* relation, while leaving the central black hole mass unchanged. Tidal stripping of the progenitors of present-day dwarf spheroidal galaxies may be an important channel through which these systems can host black hole masses comparable to the upper limits obtained in our study. However, black hole growth via momentum-driven accretion and stellar capture yields more conservative mass

estimates, broadly consistent with the predictions of the $M_\bullet$–σ_* relation.

4. Conclusions

In this work, we have constructed dynamical models of dwarf spheroidal galaxies to constrain the black hole mass in conjunction with the parameters corresponding to the dark matter halo using anisotropic distribution functions. We find that the posterior for the dark matter mass is strongly constrained with a median value between 10^8 and $10^9 M_\odot$. On the other hand, the posterior distribution for the black hole mass remains flat toward the low mass end. We derive 95% credible upper limits on the black hole masses in dwarf spheroidal galaxies, which lie in the range 10^5–$10^6\,M_\odot$. We combine the upper limits obtained in our study for dwarf spheroidal galaxies with previously reported black hole mass measurements and upper limits from the literature to derive a unified $M_\bullet$–σ_* relation spanning $\sigma_* \sim 10$–$300\,\mathrm{km\,s^{-1}}$. We find that the $M_\bullet$–σ_* relation is given by $\log(M_\bullet) = 8.32 + 4.08\log(\sigma_*/200\ \mathrm{km\ s^{-1}})$, with an intrinsic scatter of $\sigma_{\rm int} = 0.55$. We compare different formation scenarios through which the dwarf spheroidal galaxies can host central black holes consistent with the upper limits derived in our study. The upper limits on black hole masses obtained in our work ($\leqslant 10^6\,M_\odot$) are consistent with a scenario in which the progenitors of present-day dwarf spheroidal galaxies experienced tidal stripping, reducing their stellar mass while leaving the central black hole largely unaffected. We conclude that models of black hole growth via momentum-driven gas accretion and stellar capture yield black hole masses between 10^3 and $10^4 M_\odot$, closer to the prediction of $M_\bullet$–σ_* relation within the 95% credible upper limits on the black hole masses presented in this work.

Acknowledgments

The authors thank the referee for the insightful comments and questions, which have greatly helped in improving the manuscript. We gratefully acknowledge the use of the high-performance computing facility "NOVA" at the Indian Institute of Astrophysics, Bengaluru, India, where all computations were carried out. The work is supported by ANRF grant CRG/2021/005174/PHY.

ORCID iDs

K. Aditya https://orcid.org/0000-0002-1250-4359
A. Mangalam https://orcid.org/0000-0001-9282-0011

References

Aditya, K. 2024, A&A, 689, A161
Aditya, K., & Banerjee, A. 2021, MNRAS, 502, 5049
Aditya, K., Banerjee, A., Kamphuis, P., et al. 2023, MNRAS, 526, 29
Aditya, K., Kamphuis, P., Banerjee, A., et al. 2022, MNRAS, 509, 4071
Battaglia, G., & Nipoti, C. 2022, NatAs, 6, 659
Beifiori, A., Courteau, S., Corsini, E. M., & Zhu, Y. 2012, MNRAS, 419, 2497
Bellovary, J. M., Cleary, C. E., Munshi, F., et al. 2019, MNRAS, 482, 2913
Bhattacharyya, D., & Mangalam, A. 2018, JApA, 39, 1
Bhattacharyya, D., & Mangalam, A. 2020, ApJ, 895, 130
Bustamante-Rosell, M. J., Noyola, E., Gebhardt, K., et al. 2021, ApJ, 921, 107
Cappellari, M., Verolme, E. K., van der Marel, R. P., et al. 2002, ApJ, 578, 787
Ciotti, L. 2021, Introduction to Stellar Dynamics (Cambridge Univ. Press)
Cuddeford, P. 1991, MNRAS, 253, 414
Dalla Bontà, E., Ferrarese, L., Corsini, E. M., et al. 2009, ApJ, 690, 537
den Brok, M., van de Ven, G., van den Bosch, R., & Watkins, L. 2014, MNRAS, 438, 487
Ferrarese, L., & Merritt, D. 2000, ApJL, 539, L9
Foreman-Mackey, D., Hogg, D. W., Lang, D., & Goodman, J. 2013, PASP, 125, 306
Gebhardt, K., Bender, R., Bower, G., et al. 2000, ApJL, 539, L13
Gebhardt, K., Rich, R. M., & Ho, L. C. 2005, ApJ, 634, 1093
Graham, A. W. 2008, ApJ, 680, 143
Grcevich, J., & Putman, M. E. 2009, ApJ, 696, 385
Greene, J. E., Strader, J., & Ho, L. C. 2020, ARA&A, 58, 257
Gültekin, K., Gebhardt, K., Kormendy, J., et al. 2014, ApJ, 781, 112
Gültekin, K., Richstone, D. O., Gebhardt, K., et al. 2009, ApJ, 698, 198
Hayashi, K., Chiba, M., & Ishiyama, T. 2020, ApJ, 904, 45
Jardel, J. R., & Gebhardt, K. 2012, ApJ, 746, 89
Kamann, S., Wisotzki, L., Roth, M. M., et al. 2014, A&A, 566, A58
Kelly, B. C. 2007, ApJ, 665, 1489
King, A. 2003, ApJL, 596, L27
Komatsu, E., Dunkley, J., Nolta, M. R., et al. 2009, ApJS, 180, 330
Kormendy, J., & Ho, L. C. 2013, ARA&A, 51, 511
Krajnović, D., Cappellari, M., & McDermid, R. M. 2018, MNRAS, 473, 5237
Lora, V., Sánchez-Salcedo, F., Raga, A., & Esquivel, A. 2009, ApJL, 699, L113
Lützgendorf, N., Kissler-Patig, M., Neumayer, N., et al. 2013, A&A, 555, A26
Maccarone, T. J., Fender, R. P., & Tzioumis, A. K. 2005, MNRAS Lett., 356, L17
Manni, L., Nucita, A., De Paolis, F., Testa, V., & Ingrosso, G. 2015, MNRAS, 451, 2735
Mateo, M. 1998, ARA&A, 36, 435
McConnachie, A. W. 2012, AJ, 144, 4
McConnell, N. J., & Ma, C.-P. 2013, ApJ, 764, 184
McConnell, N. J., Ma, C.-P., Gebhardt, K., et al. 2011, Natur, 480, 215
McConnell, N. J., Ma, C.-P., Murphy, J. D., et al. 2012, ApJ, 756, 179
McLaughlin, D. E., Anderson, J., Meylan, G., et al. 2006, ApJS, 166, 249
Mehrgan, K., Thomas, J., Saglia, R., et al. 2019, ApJ, 887, 195
Melo-Carneiro, C. R., Collett, T. E., Oldham, L. J., et al. 2025, MNRAS, 541, 2853
Merritt, D. 1985, AJ, 90, 1027
Merritt, D. 2013, Dynamics and Evolution of Galactic Nuclei (Princeton Univ. Press)
Merritt, D., & Ferrarese, L. 2001, MNRAS, 320, L30
Muñoz, R. R., Côté, P., Santana, F. A., et al. 2018, ApJ, 860, 66
Navarro, J. F., Frenk, C. S., & White, S. D. 1997, ApJ, 490, 493
Ngo, H. N., Nguyen, D. D., Le, T. T., et al. 2025, Univ, 11, 360
Nguyen, D. D., Cappellari, M., Ngo, H. N., et al. 2025, AJ, 170, 124
Nguyen, D. D., Cappellari, M., & Pereira-Santaella, M. 2023, MNRAS, 526, 3548
Nightingale, J. W., Smith, R. J., He, Q., et al. 2023, MNRAS, 521, 3298
Osipkov, L. 1979, PAZh, 5, 77
Pacucci, F., Ni, Y., & Loeb, A. 2023, ApJ, 956, 37
Pascale, R., Binney, J., Nipoti, C., & Posti, L. 2019, MNRAS, 488, 2423
Pascale, R., Nipoti, C., Calura, F., & Della Croce, A. 2024, A&A, 684, L19
Plummer, H. C. 1911, Astronomical Society, 71, 460
Posti, L., Binney, J., Nipoti, C., & Ciotti, L. 2015, MNRAS, 447, 3060
Read, J. I., Walker, M., & Steger, P. 2019, MNRAS, 484, 1401
Reines, A. E. 2022, NatAs, 6, 26
Reines, A. E., Greene, J. E., & Geha, M. 2013, ApJ, 775, 116
Rusli, S. P., Thomas, J., Saglia, R. P., et al. 2013, AJ, 146, 45
Shchelkanova, G., Hayashi, K., & Blinnikov, S. 2021, ApJ, 909, 147
Soltan, A. 1982, MNRAS, 200, 115
Spekkens, K., Urbancic, N., Mason, B. S., Willman, B., & Aguirre, J. E. 2014, ApJL, 795, L5
Strigari, L. E., Bullock, J. S., Kaplinghat, M., et al. 2008, Natur, 454, 1096
Tadhunter, C., Marconi, A., Axon, D., et al. 2003, MNRAS, 342, 861
Thatte, N. A., Melotte, D., Neichel, B., et al. 2022, Proc. SPIE, 12184, 1218420
Thomas, J., Ma, C.-P., McConnell, N. J., et al. 2016, Natur, 532, 340
Tremaine, S., Gebhardt, K., Bender, R., et al. 2002, ApJ, 574, 740
van den Bosch, R. C. 2016, ApJ, 831, 134
van der Marel, R. P., & Anderson, J. 2010, ApJ, 710, 1063
Vasiliev, E. 2019, MNRAS, 482, 1525
Walker, M. G. 2014, JCos, 23, 10946
Walker, M. G., Mateo, M., Olszewski, E. W., et al. 2007, ApJL, 667, L53
Walker, M. G., Mateo, M., Olszewski, E. W., et al. 2009, ApJ, 704, 1274
Walsh, J. L., van den Bosch, R. C. E., Gebhardt, K., et al. 2016, ApJ, 817, 2
Wright, S. A., Jones, T., Larkin, J., et al. 2024, Proc. SPIE, 13096, 148
Yıldırım, A., van den Bosch, R. C. E., van de Ven, G., et al. 2015, MNRAS, 452, 1792